PCCP

Cite this: *Phys. Chem. Chem. Phys.*, 2011, **13**, 5441–5449

www.rsc.org/pccp

PAPER

A density functional theory approach to mushroom-like platinum clusters on palladium-shell over Au core nanoparticles for high electrocatalytic activity†‡

Sai Duan,[ab] Ping-Ping Fang,[ac] Feng-Ru Fan,[a] Ian Broadwell,[a] Fang-Zu Yang,[a] De-Yin Wu,[a] Bin Ren,[a] Christian Amatore,[c] Yi Luo,[b] Xin Xu[a] and Zhong-Qun Tian*[a]

Received 11th January 2011, Accepted 15th February 2011
DOI: 10.1039/c1cp20096h

Recently, it was found that Pt clusters deposited on Pd shell over Au core nanoparticles (Au@Pd@Pt NPs) exhibit unusually high electrocatalytic activity for the electro-oxidation of formic acid (P. P. Fang, S. Duan, *et al.*, *Chem. Sci.*, 2011, **2**, 531–539). In an attempt to offer an explanation, we used here carbon monoxide (CO) as probed molecules, and applied density functional theory (DFT) to simulate the surface Raman spectra of CO at this core-shell-cluster NPs with a two monolayer thickness of Pd shell and various Pt cluster coverage. Our DFT results show that the calculated Pt coverage dependent spectra fit the experimental ones well only if the Pt clusters adopt a mushroom-like structure, while currently the island-like structure is the widely accepted model, which follows the Volmer–Weber growth mode. This result infers that there should be a new growth mode, *i.e.*, the mushroom growth mode as proposed in the present work, for Au@Pd@Pt NPs. We suggest that such a mushroom-like structure may offer novel active sites, which accounts for the observed high electrocatalytic activity of Au@Pd@Pt NPs.

Introduction

The last two decades have witnessed substantial advances in the application of nanoparticles (NPs) in electrochemistry, especially for electrocatalysis. There have been several methods to enhance the catalytic activities of catalysts, such as shape control,[1–3] molecular modification,[4,5] and NP design with different surface compositions and surface morphologies.[6,7] Among these, the design of different kinds of NPs, which have been extended from single metal NPs to bimetallic and trimetallic NPs, has played an important role. Alloys and core-shell NPs are two kinds of the most important, and metal NPs are widely used in catalysis.[8,9] core-shell NPs, however, have their own advantages for the catalytic reactions over alloy NPs. For the former, their core diameters, shell thicknesses, sizes and elemental compositions of cores and shells are all adjustable.[8,10–12] There are several kinds of core-shell NPs, such as (1) the mono-metallic surface created by the epitaxial growth mode; (2) the bimetallic surface grown by the island growth mode; (3) and the trimetallic core-shell-cluster structure.[8,12–14] The core-shell-cluster structure is more complicated than the other two types of NPs and is thought to contain more active sites for the electrocatalysis.[15]

Platinum NPs act as remarkable catalysts for a variety of electrochemical reactions relevant to fuel cells. These include the oxidation of hydrogen,[4] formic acid,[15,16] and methanol,[1] as well as the reduction of oxygen.[4,17] Since Pt is very expensive, it is important to maximize the catalytic activity of Pt-based catalysts while trying to minimize the amount of Pt used during the reaction.[18] To this end, a common approach is to load Pt on other transition metals to form heterogeneous metal nanocatalysts. In order to take advantage of Pt-based NP systems in the design of new catalysts, a synergistic effect of the structure, chemical composition, and electronic modifications, has yet to be fully understood. Hence, the research on the growth mechanisms of Pt loading on other metals will facilitate the design and preparation of fine composite nanocatalysts. Most recently, the growth of heterogeneous metals, including Pt, has been widely studied.[3,14,19]

[a] *State Key Laboratory of Physical Chemistry of Solid Surfaces and LIA CNRS XiamENS "NanoBioChem", College of Chemistry and Chemical Engineering, Xiamen University, Xiamen 361005, China. E-mail: zqtian@xmu.edu.cn; Fax: +86 592 2183047; Tel: +86 592 2186979*
[b] *Theoretical Chemistry, School of Biotechnology, Royal Institute of Technology, S-106 91 Stockholm, Sweden*
[c] *UMR CNRS 8640 "PASTEUR" and LIA CNRS XiamENS "NanoBioChem", Ecole Normale Supérieure, Département de Chimie, Université Pierre et Marie Curie-Paris 6, 24 rue Lhomond, 75231 Paris cedex 05, France*

† Electronic supplementary information (ESI) available: Additional TEM images of the Au@Pd@Pt NPs, the bond displacement vector method for calculating relative Raman intensities. See DOI: 10.1039/c1cp20096h/

‡ This article is part of the special collection on Interfacial processes and mechanisms in celebration of John Albery's 75th birthday.

Typically, the deposition of Pt on Pd core nanocrystals can be non-epitaxially deposited *via* the Volmer-Weber (V-W) mode or epitaxially deposited *via* the Frank–van der Merwe (F-M) mode, depending on the synthesis conditions used.[13,20,21] At this moment, there are still few detailed studies on the real surface state and structure of Pt on the surface of Pd nanocrystals prepared by using the non-epitaxial routes.

Recently our group has synthesized a range of trimetallic core shell cluster NPs (TMCSCNP), which consist of a gold core, covered by a palladium shell, onto which platinum clusters are deposited (Au@Pd@Pt). These NPs show unusually high activity for the electro-oxidation of formic acid. We have previously reported our efforts toward the optimization of the catalytic activity of these TMCSCNP by tuning shell thicknesses and cluster coverage.[15] We will show here that, by combining *in situ* surface-enhanced Raman spectroscopy (SERS) measurements and density functional theory (DFT) calculations, it is possible to explore the electronic and morphological properties of TMCSCNP. Such a mission is not possible with experiments alone.[15]

In the present study, we explore the surface structure of trimetallic NPs (Au@Pd@Pt) using carbon monoxide (CO) as a probe molecule. It is well-known that the Raman shift associated with the stretching of adsorbed CO molecules is sensitive to the adsorption site and coverage of CO.[22] By simulating the Raman spectra of CO adsorbed on NPs, and comparing the theoretical results with the experiments, we aim to determine the surface structures of NPs and correlate their shapes and electronic states with their high electrocatalytic activity. A unique mushroom-like NP structure is unearthed and a new NP growth mode is, therefore, proposed.

Method of calculations and experimental details

DFT calculations

All calculations were performed using the DFT total-energy Vienna *ab initio* simulation package (VASP).[23,24] The projector augmented-wave method (PAW)[25] and the Perdew–Burke–Ernzerhof generalized-gradient approximation (GGA-PBE)[26] exchange–correlation functional were employed. The wave functions were expanded in a plane-wave basis set with an energy cut off of 400 eV. The Methfessel and Paxton method[27] was used with a temperature broadening of $k_BT = 0.01$ eV to improve convergence (k_B = the Boltzmann constant, T = temperature) and the total energy was extrapolated to 0 K. The induced dipole moment was considered by applying a dipole correction along the z-axis, which is normal to the surface.[28,29] The PAW potential was generated by taking scalar relativistic corrections into account.[25] The theoretically optimized lattice constants were 4.174 and 3.953 Å for Au and Pd, respectively. These results are in agreement with the published values, which are 4.078 Å for Au and 3.891 Å for Pd.[30]

Based on the experimental results, as will be discussed below, on pure Pd and Pt (111), CO was assumed to adsorb on a Pd bridge site and a Pt atop site with an upright adsorption mode. During geometry optimization, we allowed the CO molecule and all other metal atoms to relax in the z direction (normal to the atop surface), while the bottom two layers of the slab were fixed in the position of the optimized bulk metal. The final forces on the atoms were less than 0.02 eV/Å. It is well known that GGA-PBE has a tendency to underestimate the vibrational frequencies.[31] Due to the lack of proper description of anharmonicity and the use of approximate DFT functional, a scaling factor is often used to make correction of the calculated frequency.[32] In the present work, according to the calculation for a free CO molecule, a uniform scaling factor of 1.023 was found to scale all calculated C–O stretching (ν_{CO}) frequencies upon adsorption. This scaling factor is in good agreement with that found in previous calculations.[32] The relative Raman intensities were calculated by the so-called bond displacement vector method (see ESI for details). To compare with the experimental spectra, the calculated relative Raman intensities were broadened by a Lorentzian function with a full width at the half-maximum (fwhm) of 30 cm^{-1}.

In the course of calculations, we have tested various adsorption patterns of CO on the Pd(111) surface and found that CO adsorbed on bridge sites with the pattern of c(4×2) giving perfect CO stretching frequencies as compared with experimental observations. Hence, such c(4×2) super-cell structures were used to simulate Au@2Pd and Au@2Pd@xPt. Here Au@2Pd stands for Au@Pd NPs with 2 monolayers of Pd and x in Au@2Pd@xPt represents the stoichiometric Pt coverage θ_{Pt}. These are the experimental systems we are going to simulate. The details of the model set-up will be given in the following sections as appropriate. For the smallest super-cell, the k-point sampling used in calculations was a 4×4×1 mesh of Monkhorst–Pack grids[33] generated from four special reciprocal k points in the irreducible Brillouin zone (IBZ) for the Brillouin zone integration. Larger super-cells used fewer k points for the Brillouin zone integration, which were determined by the length of lattice vectors of the super-cells.

Experimental sections

Electrochemical measurements were conducted using a CHI 631B electrochemical workstation (CH Instruments, China). Raman spectra were recorded on a LabRam I confocal microprobe Raman system (Jobin-Yvon, France). The excitation wavelength was 632.8 nm from a He–Ne laser, with a power of about 4 mW on the sample.

A spectroelectrochemical cell containing a Pt wire and a saturated calomel electrode (SCE) serving as the counter and the reference electrodes respectively, were used for both the electrochemical and the *in situ* spectroelectrochemical SERS measurements.[34] All potentials given in this work are relative to an SCE. Glassy carbon (GC), covered with NPs, acted as the working electrode. A GC disk electrode with diameter = 3 mm was used as the support. It was prepared for use by mechanical polishing with successively finer grades of 3 to 0.05 μm alumina powder (Buehler Ltd., USA) to achieve a mirror-like finish. The GC electrode was then cleaned by sonication in Millipore water for 3 min after each polishing step. Following polishing it was electrochemically cleaned in 0.5 M H_2SO_4 by scanning through the potential −0.25 to 1.25 V at 500 mV/s for 10 min. The Au@Pd and Au@Pd@Pt NPs

were synthesized as described by our previous work as in ref. 15. Essentially a sol containing Au seeds with a diameter of about 55 nm was created based on Frens' method.[35] Monolayers of Pd were then deposited using aqueous solutions of H_2PdCl_4.[15] Pt islands were also deposited chemically using H_2PtCl_6. Finally active surface area of the working electrode was determined by hydrogen adsorption/desorption and confirmed by oxygen adsorption/desorption as in the literature.[6,36–38]

Results and discussions

SERS and electrochemical study

The schematic structures of Au@Pd@Pt core-shell-cluster NPs are depicted in Fig. 1a. The yellow part represents the Au core, the black part stands for the Pd shell and the Pt clusters are represented by dark blue dots. Fig. 1b displays the linear voltammograms obtained from ~55 nm Au@2Pd and Au@2Pd@xPt NPs in a solution of 0.1 M HCOOH + 0.1 M H_2SO_4 (see ref. 15 for details). A high measured current indicates a high catalytic activity for the electro-oxidation of formic acid. As compared with the results of Au@2Pd (black line in Fig. 1b), depositions of Pt clusters, with various stoichiometric Pt coverage (*i.e.* θ_{Pt}) ranging from 30–70%, all increase the activity. As indicated by the red line in Fig. 1b, the NPs with Pt coverage of 50% show the highest catalytic activity for the oxidation of formic acid. Such a high electro-catalytic activity of the trimetallic NPs should be related to a specific structure. Nevertheless, this phenomenon has not yet been explored before.[15]

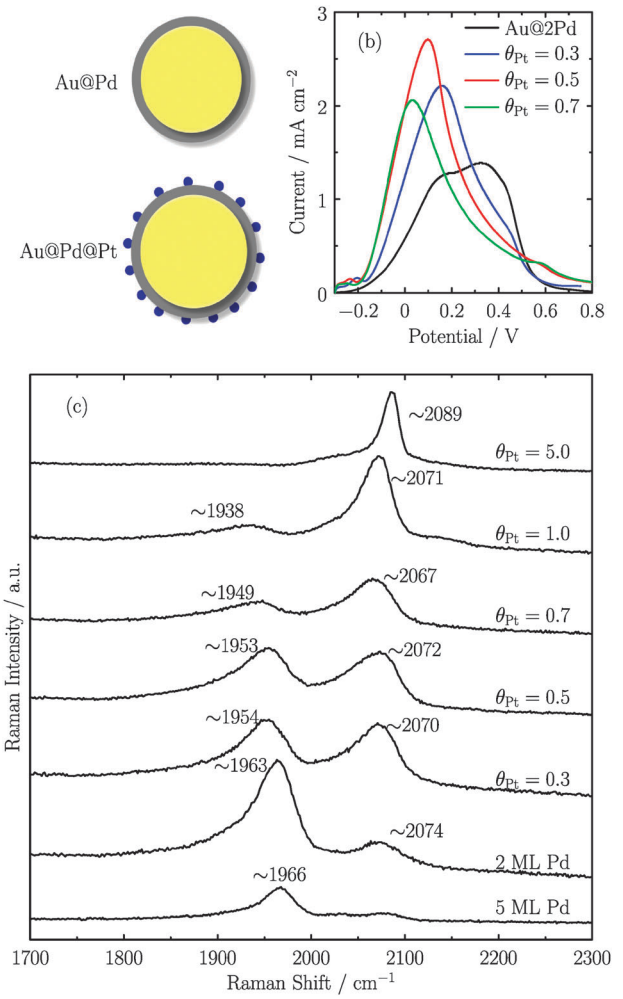

Fig. 1 (a) Schematic structures of Au@Pd and Au@Pd@Pt NPs. (b) Linear voltammograms were obtained from 55 nm Au@Pd@Pt NPs with 2 monolayers of Pd and various θ_{Pt} in a solution of 0.1 M HCOOH + 0.1 M H_2SO_4. The scanning rate was 50 mV s^{-1}. (c) SERS spectra of CO adsorbed on 55 nm diameter core Au@Pd@Pt NPs with 2 monolayers of Pd and different stoichiometric θ_{Pt}, and SERS spectra of CO adsorbed on 55 nm diameter core Au@Pd NPs with different Pd shell thickness in a CO-saturated 0.1 M aqueous solution of $HClO_4$ at 0 V. Part of the spectral data are taken from our previous work as shown in ref. 15.

Since Raman spectroscopy is very sensitive to the surface structure, it was chosen here to investigate the basis for the high catalytic activity shown in Fig. 1b. Indeed, Fig. 1c shows that the experimental ν_{CO} changes as the thickness of the Pd shell and Pt coverage are changed. The first peak which appears at 1938–1966 cm^{-1} is assigned to the C–O stretching mode of the bridge-bonded CO molecules on the NPs. The second peak at 2060–2090 cm^{-1} is assigned to the C–O stretching mode of the atop CO molecules.[39,40] For the Pd shell with no Pt clusters present, it can be seen that the signal for the bridge-site adsorbed CO reduces significantly and that for the atop-site CO almost disappears completely when the thickness of the Pd shell changes from 2 to 5 monolayers. Also the increase in Pd shell thickness causes a Raman frequency shift for the bridge-bonded CO from 1963 to 1966 cm^{-1}. We would like to have an understanding for this phenomenon.

Fig. 1c also displays a decrease in frequency from 1963 to 1954 cm^{-1} for the bridge-bonded CO. This marks the transition from bimetallic to trimetallic NPs with Pt coverage of 0.3. As Pt coverage increases from 0.3 to 1.0, the frequency red-shifts from 1963 to 1938 cm^{-1}. Interestingly, for the atop site CO, both red and blue shifts are observed with increase of Pt coverage on Pd. Previously, such a C–O stretching frequency changes observed on Au@Pd@Pt NPs were not explained in detail. Here we performed a systematic DFT study to explain this phenomenon more thoroughly.

Epitaxial structure

Previous studies showed that Pd layers can be epitaxially coated on Au surfaces with negligible pinholes in Au@Pd NPs.[14] Here we simulate the epitaxial structure of Au@Pd and focus on the CO adsorption on the Pd shells.

For our periodic DFT calculations, it is necessary to assume a realistic surface pattern of CO on the Pd surface. In ultra-high vacuum (UHV) conditions, CO is known to adsorb on the face centered cubic (fcc) hollow site[22,41–44] and the frequency of CO stretching was found to be below 1900 cm^{-1} for low coverages.[45–47] DFT calculations from other authors have also shown that the hollow site is the most energetically favorable adsorption site when CO is adsorbed on the Pd surfaces at coverage less than 0.33.[32,48,49] Increasing the CO coverage to 0.5 leads to a pattern of c(4×2).[22,32,41–43,49–51] With this condition, low-energy electron diffraction (LEED)

results have also supported that CO molecules adsorbed on the hollow sites.[42] Recently, however, scanning tunneling microscope (STM) investigations showed that the adsorption site of CO can also turn to be the bridge site.[43] DFT calculations suggested that adsorptions on hollow sites and bridge sites possess very similar stability.[32,49] This small difference might lead to their simultaneous coexistence for forming CO adsorption patterns. In UHV conditions, the corresponding frequencies of CO were blue-shifted to around 1950 cm^{-1} at coverage of 0.5.[46,47,52] Further increasing the coverage to 0.75 yielded a pattern of $p(2\times2)$.[32,43,45–47,53,54] At this coverage, $p(2\times2)$ contained one atop site and two hollow adsorption sites which resulted in a splitting of frequencies for CO stretching modes into two bands. This is, however, not observed in our experimental condition[15] (see Fig. 1c). In electrochemical situations, infrared spectra indicated that CO molecules prefer to adsorb on bridge sites.[39]

After experimenting with various adsorbed patterns of CO on the Pd surface, we found that CO adsorbed on bridge sites with a pattern of c(4×2) can give perfect CO stretching frequencies as compared with experimental observations (see Table 1). The scaled C–O frequency with the highest intensity was calculated to be 1968.0 cm^{-1}, which is in good agreement with experimental values of ~1966 cm^{-1} (see Fig. 1c for plots with 5 ML Pd and 20 ML Pd). Hence, the pattern of c(4×2) was taken as the unit cell and super cell sizes to build theoretical configurations of CO adsorbed on Pd, as well as on Au@Pd surfaces (*cf.* Fig. 2a).

For Au@2Pd, a super-cell containing 2 c(4×2) Au (111) layers and 2 c(4×2) Pd (111) layers were thus chosen in accordance with the CO adsorption pattern. Increasing the number of layers of Au(111) from 2 to 4 was found to change the calculated vibrational frequency of adsorbed CO by less than 1 cm^{-1}, which verifies the present model. Due to the epitaxial growth nature of Au@2Pd, the optimized Au lattice constant was used in simulating Au@2Pd NPs. Au@*n*Pd NPs were represented by a super-cell containing 2 c(4×2) Au (111) layers and 4 c(4×2) Pd (111) layers, while the latter adopted the optimized Pd lattice constant. Such a choice echoes the experimental finding that there existed no frequency shift, as compared to that on pure Pd, when CO was adsorbed Pd shell thicker than 5 monolayers.

In order to assess whether 4 layers was thick enough to accurately model the thicker Pd shells (*i.e.* ≥ 5 ML) we reduced the four Pd slab layers to just two in the model, but keeping the interlayer distance fixed at the four Pd slab optimized with CO adsorption. We found that such a fixed 2 layer model predicts that the scaled CO stretching frequency of adsorbed CO molecules on pure Pd is 1967.3 cm^{-1}. This is in perfect agreement with that of the 4 layer slab model, indicating that as long as the inter slab layer distance is correctly preserved (geometric effect), even a 2 layer model can be a good model to simulate CO adsorption on pure or very thick layers of Pd shell. Table 1 shows that this is not the case for Au@2Pd: removing the 2 bottom layers of Au and keeping the 2 top layers of Pd fixed at the interlayer distance of Au@2Pd upon CO adsorption lead to a frequency shift of ~8 cm^{-1} (1933 *vs.* 1941 cm^{-1}, see Table 1). Apparently, the Au core has two effects on the epitaxial Pd shell. The first effect is electronic, which arises from a difference in the work functions between the Au and Pd. This effect is thought to give the frequency shift of ~8 cm^{-1} for Au@2Pd. The second effect is the geometric effect. When Pd is epitaxially grown on Au, the distance between Pd atoms is larger than that in pure Pd, as Au has a larger lattice constant than Pd (calc. 4.174 *vs.* 3.953 Å). As shown in Table 1, when the results of the fixed 2 slab layer models are compared, there is a red shift of 34 cm^{-1} for CO molecules adsorbed on the pure Pd and the Au@2Pd. This can be attributed to the geometric effect. The large frequency shift signifies the importance of the geometric effect, which is probably the reason that Au@2Pd NP surfaces have already shown a higher electrocatalytic activity to electro-oxidation of formic acid as compared to pure Pd.[15]

Our calculation results also show that the dipole moment between Au and Pd layers is around −0.20 Debye nm^{-2}. Here the negative sign means that the electrons transfer from bottom Au layers to top Pd layers. The combine effects of electronic and geometric phenomena can be seen in Table 1 for the 4 slab layer model. A red shift from the pure Pd to the Au@2Pd of 27 cm^{-1} is observed. This red shift tendency is consistent with the experimental measurements as shown in Fig. 1c. It should be pointed out that the predicted 1941 cm^{-1} peak is too low as compared to the experimental value of 1963 cm^{-1}. We assumed a 0.5 CO coverage with a c(4×2) pattern based on the experimental results on pure Pd. The CO coverage on Au@2Pd may be higher due to the increased Pd–CO π-backdonation. However, increasing CO coverage will lead to increased dipole–dipole interaction between adsorbed CO molecules, which, in turn, will weaken the metal–CO bond, and reduce the π-backdonation, leading to a blue-shift of ν_{co}. As we will show below, the CO–CO dipole–dipole interaction is a key factor that influences the SERS spectra. However, increasing CO coverage from 0.5 with a c(4×2) pattern to 0.514 with a ($\sqrt{3}\times35$) pattern will dramatically lead to increase of the super-cell by 17 times,[51] which is computationally very expensive. Hence, we preserve the 0.5 CO coverage with a c(4×2) pattern for all our calculations presented here.

Table 1 DFT calculated frequencies in cm^{-1} for CO adsorbed on pure Pd surfaces and Au@2Pd NPs. Pure Pd surfaces are represented by 4 layers of Pd (111) surface and Au@2Pd NPs 2 layers of Au (111) with 2 layers of Pd (111) surfaces. The fixed two layers indicated the artificial models of that removing two bottom layers in the models of pure Pd surfaces and Au@2Pd NPs then fixing other 2 layers. The CO adsorbed on bridge sites with the pattern of c(4×2)

	4 layers		Fixed 2 layers	
Species	Freq.	Scal. freq.	Freq.	Scal. freq.
Pure Pd	1923.8	1968.0	1923.1	1967.3
Au@2Pd	1897.4	1941.1	1889.9	1933.4

Island structure

We are now in the position to discuss how ν_{CO} frequencies shift with increasing Pt coverage on Au@2Pd.

For CO adsorption on Pt surfaces, the adsorption prefers the atop sites in UHV conditions at low coverage.[51]

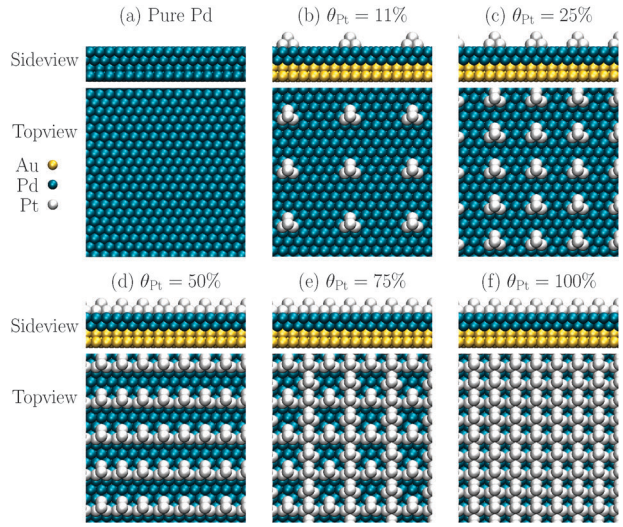

Fig. 2 Topview (up) and sideview (bottom) of the calculated configurations used to simulate island-like structure model for different stoichiometric Pt coverage θ_{Pt}. (a): Pure Pd surfaces, (b): θ_{Pt} = 11%, (c): θ_{Pt} = 25%, (d): θ_{Pt} = 50%, (e): θ_{Pt} = 75%, and (d): θ_{Pt} = 100%. Yellow, dark blue and white balls represent Au, Pd and Pt atoms, respectively. All Pt atoms are assumed to form Pt_4 pyramid clusters and adsorb on Pd surface with one basal plan of each pyramid.

Experimental observations from the literature showed that atop sites are also the favorable adsorption sites even at higher coverage in electrochemical conditions.[40] There is a well-known problem with GGA type of DFT calculations, which predict that the hollow sites are the more energy favorable adsorption sites.[55,56] Here, we have to adjust our models to restrict the CO adsorption sites at Pt atop sites in the theoretical calculations. This will not impose a problem if ν_{CO} frequencies are our main concern.

According to the regular V-W growth mode,[57] we considered that Pt atoms form a pyramid structure adsorbed on Pd surfaces. In our calculations, the pyramid Pt structure was represented by Pt_4 clusters. A series of θ_{Pt} values were tried to form patterns of Pt_4 clusters adsorbed on Au@2Pd NPs. Fig. 2b–f display the patterns with θ_{Pt} values of 11%, 25%, 50%, 75%, and 100%, respectively. These patterns were generated by expanding the c(4×2) unit-cell to 3×3, 2×2, 2×1, 2×2, 1×1 with 1, 1, 1, 3, 1 Pt_4 clusters, respectively. From these patterns, it can be seen that the Pt_4 clusters are homogeneously distributed and areas of Pt aggregation are ignored. This is not an unrealistic assumption. If Pt aggregation can not be ignored, there will always be large Pd areas such that ν_{CO} decrease for CO adsorption on Pd will not be observed with increasing θ_{Pt}. This is, however, not in accordance with the experimental results shown in Fig. 1c. This suggests Pt atoms can not aggregate to form large area of Pd shell. If we keep the Pt_4 as a unit of Pt clusters, when θ_{Pt} increases to 50%, the Pt_4 clusters are no longer separate 0-D nanostructures but come into contact. At this point clusters appear as 1-D nanostructures on the Pd surface.

From the modelling, it was found that the best fit for CO adsorption patterns on the Au@Pd@Pt surfaces was similar to that on pure Pd and Au@Pd, which was c(4×2). In this island structure model, CO was again adsorbed on Pd bridge sites and Pt atop sites.

The calculated Raman spectra for the island structure models at different θ_{Pt} are shown in Fig. 3. By using scaled data, we are able to directly compare calculated results with the experimental data. By comparing Fig. 1c and Fig. 3, we can see similarities in the plots with peaks appearing at 1900 cm^{-1} and 2100 cm^{-1}, corresponding to bridge bonded and atop bonded CO, respectively. On the other hand, discrepancy between experiments and theory is also evident. For the bridge bonded CO spectra, as θ_{Pt} is increased from 0 to 25% the frequency red-shifts by 36 cm^{-1}. This shift dramatically increases to ~92 cm^{-1} even at mid coverage θ_{Pt} = 50%. This very large red-shift is in clear disagreement with experimental data where ν_{CO} red-shifts only by ~ 10 cm^{-1} (see Fig. 1c). Furthermore, for CO adsorbed on Pt atop sites, the calculated ν_{CO} uniformly blue shifts with increasing θ_{Pt}. This is also not consistent with experimental observations shown in Fig. 1c, where both blue- and red-shifts were observed.

The rapid red-shift behaviour of calculated frequencies from PdC–O stretching can be attributed to two factors. The first one is that the deposited Pt_4 clusters can block the dipole–dipole coupling between CO molecules adsorbed on the Pd surface. The other one is the charge transfer effect from Pd to C–O antibonding π orbitals. The dipole moment between the Pt clusters and the Au@2Pd NPs is calculated to be +0.88 Debye nm^{-2} for θ_{Pt} = 100%. This is 4.4 times larger than the calculated dipole moment between Au core and Pd shell in Au@2Pd NPs. Here the positive sign denotes that the direction of electron transfer is from the top Pt cluster to the underlying Au@2Pd NPs. Such a charge transfer effect is

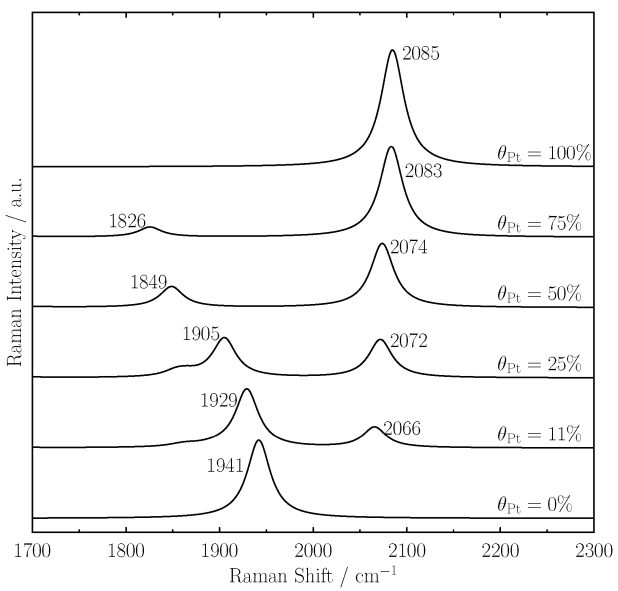

Fig. 3 Calculated Raman spectra of CO adsorbed on island-like structure Au@2Pd@*x*Pt NPs of different stoichiometric Pt coverage θ_{Pt}. The CO adsorbed on Pd bridge sites with the best fit of c(4×2) pattern and adsorbed on Pt atop sites with all possible positions. The calculated frequencies are scaled by a factor 1.023 and relative intensities are calculated by the bond displacement vector method. The numbers given in each line indicate the corresponding peak positions.

beneficial to Pd–CO bonding and becomes more and more significant as the Pt_4 coverage increases, leading to steady red-shift of ν_{CO} for PdC–O. It is important to note that the block effect can already be quite significant even when only a few Pt clusters are deposited on the Pd shell, where the charge transfer effect is not important. The dipole moment between the Pt clusters and the Au@2Pd NPs is calculated to be less than +0.10 Debye nm^{-2} for θ_{Pt} = 11% and 25%. Nevertheless, from Fig. 3, as compared to that at θ_{Pt} = 0%, large red-shifts of 12 and 36 cm^{-1} can already be seen for θ_{Pt} = 11% and 25% for the bridge bonded CO. So we suggest that there is a synergistic effect of both factors, leading to a too rapid red shift, as opposed to the experimental observations.

It has to be admitted that our choice of Pt_4 clusters seems arbitrary. The quantity of how much the red-shift might be can be different for different size of the Pt clusters. But as long as the island structure of the Pt clusters is maintained, which effectively blocks the dipole–dipole coupling between CO molecules, the qualitative picture for rapid red-shifts of ν_{CO} will remain the same, which contradicts to the experiment and calls for new structure model for deposition of the Pt clusters on the Pd shell.

Mushroom structure

From the Island structure model we have seen that the experimental data does not agree with calculated results for frequency shifts of CO adsorbed on either bridge bonded sites or atop sites. In this section we will propose a new Pt structure model which is thought to exist during trimetallic NPs synthesis.

In the previous model, when the stochiometric coverage θ_{Pt} is increased, the real coverage (contact between surfaces) increases rapidly which decreases the dipole–dipole coupling between adsorbed CO molecules rapidly. In order to avoid this situation, it is necessary to increase the real coverage in the model more slowly. This is achieved by using a cluster with a mushroom-like structure, which has a narrow base and a wide body. The detailed structures which are chosen for this part of the study are shown in Fig. 4a–c. In this structure, Pt atoms form a small basal precursor where cluster growth starts from. In the mushroom model for the present calculations, we consider this precursor as a Pt_3 or Pt_5 planar cluster which is adsorbed on a super cell of 3×3, being an integer multiple expansion of the c(4×2) unit-cell of Au@2Pd surfaces. We recall that, according to the Volmer–Weber growth mode, we normally expect a regular pyramid of Pt clusters. Note that, the details of a mushroom structure may differ, but the key in such a structure is that the real coverage of the first Pt layer is about the same for almost all θ_{Pt} values when θ_{Pt} = 0.2–0.7 as shown in Fig. 4. The large cohesive energy of Pt provides a reason why the mushroom structure is stable on Au@2Pd NPs. We expect that this structure can guarantee that the frequencies of PdC–O stretching remain in the high frequency region.

In this model, as with previous models, we keep the largest CO adsorption pattern as c(4×2) and also keep CO molecules adsorbed on Pd bridge sites with the largest fitting of the pattern. Similarly, CO is also adsorbed on all possible Pt atop sites. The calculated Raman spectra of this mushroom model are all scaled and broadened in the same way as outlined earlier in the DFT calculations section. The results are shown in Fig. 4d.

For the bridge bonded CO on Pd (at a frequency *ca.* 1900 cm^{-1}, Fig. 4d), the calculated results show that when θ_{Pt} increases the frequency changes slightly. As expected, the largest calculated red-shift is only 34 cm^{-1} even when θ_{Pt} is near 60%. This is much smaller than the red-shift in the island model of almost 100 cm^{-1} at θ_{Pt} = 50%. The much smaller red-shift calculated from the mushroom structure model is in much better agreement with experimental observations (Fig. 1c). As with the mushroom structure model the dipole–dipole coupling between CO adsorbed on Pd is almost all the same irrespective of θ_{Pt} coverage, the calculated red-shift can be attributed to electron transfer between Pt mushroom clusters and Au@2Pd NPs. The calculated dipole moments indicate that charge transfer between the Pt mushroom clusters and Au@2Pd NPs is 7 times larger at θ_{Pt} = 58% than at 39%. The calculated data for the Pt atop adsorbed CO (shown as the peaks in Fig. 4d *ca.* 2100 cm^{-1}) first decrease then increase with increasing θ_{Pt}. This is also observed in the experimental data (Fig. 1c). This change can be explained by the interactions between adsorbed CO molecules. When only one CO molecule is adsorbed at the Pt atop site, the interaction between the adsorbed CO on Pt and the adsorbed CO on Pd surface is reduced. As a result, the frequencies of PtC–O stretching red-shifts at θ_{Pt} = 39% and 47%. When θ_{Pt} = 58%, the local CO coverage is increased which strengthens the interactions between CO molecules adsorbed on Pt surfaces. Hence, the PtC–O stretching frequencies blue-shifts. Furthermore, the calculated Raman peaks show the low frequency-tail for both PdC–O and PtC–O stretching modes, which are also in agreement with experimental results.

It is also interesting to notice that the widths of the Raman bands shown in Fig. 1c change dramatically with θ_{Pt}. It is common to correlate the widths with the distribution of the various kinds of local environments for the adsorbed species acting as the probed molecules. For θ_{Pt} = 5.0, pure Pt surface is encountered to provide uniformly distributed atop sites for adsorbed CO, which correlates to the narrow CO stretching peak. For θ_{Pt} = 0.3–0.7, more complex Pt clusters exist, which offers rich active sites with different local environments for CO adsorption. Hence the significantly wider widths for θ_{Pt} = 0.3–0.7 also support the plausible existence of the unique mushroom structure instead of regular pyramid (or simple island) shape.

Comparing the theoretical and experimental Raman spectra, we conclude that the mushroom structure is likely to occur in the Au@2Pd@*x*Pt NPs. Due to the high cohesive energy associated with Pt, we suspect it is also very likely that Pt atoms may follow the mushroom structure growth mode on many other surfaces.

Different growth modes

In general, there are three different types of growth modes which are widely used in thin film growth studies and the synthesis of core-shell NPs.[57] These are (1) layer-by-layer growth (F-M mode); (2) island growth (V-W mode); and (3) S-K mode. The layer-by-layer growth (F-M mode) will

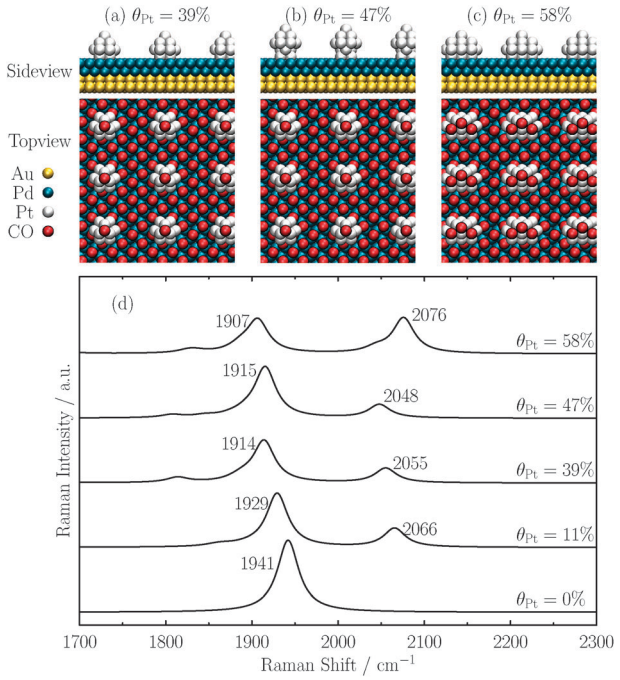

Fig. 4 (a)–(c): Topview (up) and sideview (bottom) of the calculated configurations used to simulate CO adsorbed on mushroom-like structure Au@2Pd@*x*Pt NPs of different stoichiometric Pt coverage θ_{Pt}. (a) θ_{Pt} = 39%, (b): θ_{Pt} = 47%, and (c) θ_{Pt} = 58%. Yellow, dark blue and white balls represent Au, Pd and Pt atoms respectively. Black-red spots represent the topview of CO molecules. In the sideview, CO molecules are blanked for the purpose to clearly show the mushroom growth mode. (d) Calculated Raman spectra of CO adsorbed on mushroom growth Au@2Pd@*x*Pt NPs of different θ_{Pt}. The CO adsorbed patterns are shown in topview. The calculated frequencies are scaled by a factor 1.023 and relative intensities are calculated by the bond displacement vector method. The numbers given in each line indicate the corresponding peak positions.

occur if the mismatch between the deposited material and the substrate material is small, and sum of surface energy (*i.e.* half of cohesive energy) of the substrate material and interfacial energy is larger than the surface energy of the deposited material.[57] In the opposite case, where the deposited atoms are more strongly bound to each other than they are to the substrate, this known as the island growth (V-W mode). Between the F-M and V-W modes exists the S-K mode, which is also known as "layer-plus-island growth". In the S-K mode, the growth initially follows the epitaxial layer mode. Beyond a critical layer thickness, the island growth mode takes over as the major growth mode.

In our system, it is clear that Pd adopts epitaxial growth on the surface of Au core while the growth of Pt on the Pd shell is the cluster growth. However, the spectra and calculated results show that the growth mode of Pt on Pd is different from the traditional model of island growth, which is named mushroom growth and is shown in Fig. 5. This approach would be attributed to the large cohesive energy of Pt and the experimental conditions during this synthesis process. The calculated and experimental[58] cohesive energies of Au, Pd and Pt metals are listed in Table 2. Pt has the highest cohesive energy among them and this should be the main reason for forming the Pt mushroom shaped nanoclusters. It should be noted that Pt could epitaxially grow on Pd NPs in some special cases.[13,20] We believe, however, that the Pt atoms have followed the new mushroom growth mode on Au@Pd surfaces and so provide higher electrocatalytic reactions due to the existence of more active sites involving the Pt cluster and the Pd surface.

Conclusions

In this study we have combined SERS spectra and DFT calculations to investigate the behaviour of CO molecules

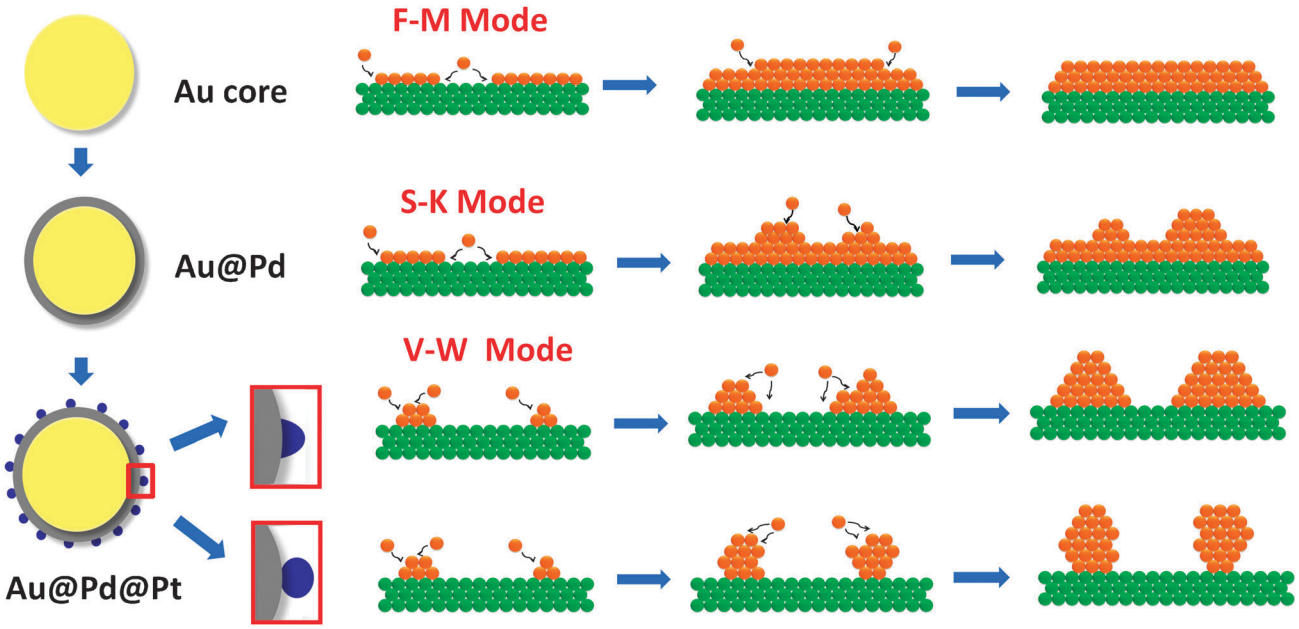

Fig. 5 Schematic figures for different growth modes.

Table 2 DFT calculated and experimental[58] cohesive energy in eV of different metals

	Au	Pd	Pt
Calc.	2.98	3.70	5.45
Expt.	3.81	3.89	5.84

adsorbed on Au-core@Pd-shell@Pt-cluster NPs. Experimental spectra have shown that the frequencies of the PdC–O stretching mode are red-shifted when θ_{Pt} is increased. The frequencies of another vibrational mode, *i.e.* the PtC–O stretching mode, undergoes a red-shift and then a blue-shift process when θ_{Pt} is increased. To explore the structures of Au@Pd@Pt NPs with atomic-level detailed we have used two kinds of chosen models for Pt islands. One is the regular Volmer–Weber growth Pt clusters which form a pyramid shape. Another one is the novel mushroom structure of Pt clusters. Comparing the theoretical Raman spectra with experimental SERS spectra, we have found that the calculated spectra of the latter model can fit the main experimental features very well whereas the former can not. Consequently we propose here that the mushroom growth mode as a new model for high cohesive energy metal atoms, such as Pt, growing on other metal surfaces. In comparison with the regular pyramid (or island) shape Pt clusters, the mushroom-shaped clusters can provide novel active sites having more coordinate number favourable for specific reactions. This may be the reason of high electrocatalytic activities of Au@Pd@Pt[15] and Pd@Pt NPs.[59–61]

For further work, we aim to introduce more tunable factors when synthesizing NPs for enhancing electrocatalytic activities. Directly extending our approach is using high index surfaces of Au core NP, which will make the Pt shell have high index surface. The mushroom-shaped Pt clusters grew on such a surface could enhance electrocatalytic activities further. Another way is using alloying as alloyed metal surfaces and mushroom clusters to bring several components (*e.g.*, Au, Pd, Pt and Ru) of active sites. This could open a new way for designing new catalysts beyond trimetallic NPs.

Acknowledgements

This work was supported by NSF of China (Nos. 20620130427, 20873114, 21033007), the Ministry of Science and Technology (Nos. 2011CB808504 and 2007CB815303). The high performance computational center of Xiamen University and the Swedish National Infrastructure for Computing (SNIC) are acknowledged for computer time.

References

1 N. Tian, Z.-Y. Zhou, S.-G. Sun, Y. Ding and Z. L. Wang, *Science*, 2007, **316**, 732–735.
2 K. M. Bratlie, H. Lee, K. Komvopoulos, P. Yang and G. A. Somorjai, *Nano Lett.*, 2007, **7**, 3097–3101.
3 Y. Xia, Y. Xiong, B. Lim and S. E. Skrabalak, *Angew. Chem., Int. Ed.*, 2008, **48**, 60–103.
4 D. Strmcnik, M. Escudero-Escribano, K. Kodama, V. R. Stamenkovic, A. Cuesta and N. M. Markovic, *Nat. Chem.*, 2010, **2**, 880–885.
5 I. Hatay, B. Su, M. A. Mendez, C. Corminboeuf, T. Khoury, C. P. Gros, M. Bourdillon, M. Meyer, J. M. Barbe, M. Ersoz, S. Zalis, Z. Samec and H. H. Girault, *J. Am. Chem. Soc.*, 2010, **132**, 13733–13741.
6 H. J. Lee, S. E. Habas, G. A. Somorjai and P. D. Yang, *J. Am. Chem. Soc.*, 2008, **130**, 5406–5407.
7 F. J. Vidal-Iglesias, J. Solla-Gullón, E. Herrero, A. Aldaz and J. M. Feliu, *Angew. Chem., Int. Ed.*, 2010, **49**, 6998–7001.
8 L. Wang and Y. Yamauchi, *J. Am. Chem. Soc.*, 2010, **132**, 13636–13638.
9 F. Tao, M. E. Grass, Y. W. Zhang, D. R. Butcher, J. R. Renzas, Z. Liu, J. Y. Chung, B. S. Mun, M. Salmeron and G. A. Somorjai, *Science*, 2008, **322**, 932–934.
10 J. T. Zhang, Y. Tang, L. Weng and M. Ouyang, *Nano Lett.*, 2009, **9**, 4061–4065.
11 J. Luo, L. Wang, D. Mott, P. N. Njoki, Y. Lin, T. He, Z. Xu, B. N. Wanjana, I. I. S. Lim and C. J. Zhong, *Adv. Mater.*, 2008, **20**, 4342–4347.
12 W. Schartl, *Nanoscale*, 2010, **2**, 829–843.
13 B. Lim, J. G. Wang, P. H. C. Camargo, M. J. Jiang, M. J. Kim and Y. N. Xia, *Nano Lett.*, 2008, **8**, 2535–2540.
14 F.-R. Fan, D.-Y. Liu, Y.-F. Wu, S. Duan, Z.-X. Xie, Z.-Y. Jiang and Z.-Q. Tian, *J. Am. Chem. Soc.*, 2008, **130**, 6949–6951.
15 P. P. Fang, S. Duan, X. D. Lin, J. R. Anema, J. F. Li, O. Buriez, Y. Ding, F. R. Fan, D. Y. Wu, B. Ren, Z. L. Wang, C. Amatore and Z. Q. Tian, *Chem. Sci.*, 2011, **2**, 531–539.
16 Q. Yuan, Z. Zhou, J. Zhuang and X. Wang, *Chem. Commun.*, 2010, **46**, 1491–1493.
17 J. Zhang, K. Sasaki, E. Sutter and R. R. Adzic, *Science*, 2007, **315**, 220–222.
18 S. Uhm, H. J. Lee, Y. Kwon and J. Lee, *Angew. Chem., Int. Ed.*, 2008, **47**, 10163–10166.
19 S. E. Habas, H. Lee, V. Radmilovic, G. A. Somorjai and P. Yang, *Nat. Mater.*, 2007, **6**, 692–697.
20 M. Jiang, B. Lim, J. Tao, P. H. C. Camargo, C. Ma, Y. Zhu and Y. Xia, *Nanoscale*, 2010, **2**, 2406–2411.
21 Z. Peng and H. Yang, *Nano Today*, 2009, **4**, 143–164.
22 A. M. Bradshaw and F. M. Hoffmann, *Surf. Sci.*, 1978, **72**, 513–535.
23 G. Kresse and J. Furthmuller, *Phys. Rev. B: Condens. Matter*, 1996, **54**, 11169–11186.
24 G. Kresse and D. Joubert, *Phys. Rev. B: Condens. Matter Mater. Phys.*, 1999, **59**, 1758–1775.
25 P. E. Blochl, *Phys. Rev. B: Condens. Matter*, 1994, **50**, 17953–17979.
26 J. P. Perdew, K. Burke and M. Ernzerhof, *Phys. Rev. Lett.*, 1996, **77**, 3865–3868.
27 M. Methfessel and A. T. Paxton, *Phys. Rev. B*, 1989, **40**, 3616–3621.
28 J. Neugebauer and M. Scheffler, *Phys. Rev. B: Condens. Matter*, 1992, **46**, 16067–16080.
29 G. Makov and M. C. Payne, *Phys. Rev. B: Condens. Matter*, 1995, **51**, 4014–4022.
30 D. R. Lide, *CRC Handbook of Chemistry and Physics*, Boca Raton, 87 edn, 2007.
31 W. Koch and M. C. Holthausen, *A Chemist's Guide to Density Functional Theory*, Wiley-VCH Verlag GmbH, 2001.
32 D. Loffreda, D. Simon and P. Sautet, *Surf. Sci.*, 1999, **425**, 68–60.
33 H. J. Monkhorst and J. D. Pack, *Phys. Rev. B: Solid State*, 1976, **13**, 5188–5192.
34 B. Ren, X. F. Lin, Y. X. Jiang, P. G. Cao, Y. Xie, Q. J. Huang and Z. Q. Tian, *Appl. Spectrosc.*, 2003, **57**, 419–427.
35 G. Frens, *Nat. Phys. Sci.*, 1973, **241**, 20–22.
36 X. Li and I. M. Hsing, *Electrochim. Acta*, 2006, **51**, 3477–3483.
37 L. Xiao, L. Zhuang, Y. Liu, J. Lu and H. D. Abrua, *J. Am. Chem. Soc.*, 2009, **131**, 602–608.
38 O. Ghodbane, L. Roue and D. Belanger, *Chem. Mater.*, 2008, **20**, 3495–3504.
39 S. Zou, R. Gomez and M. J. Weaver, *J. Electroanal. Chem.*, 1999, **474**, 155–166.
40 S.-C. Chang and M. J. Weaver, *J. Chem. Phys.*, 1990, **92**, 4582–4594.
41 H. Conrad, G. Ertl and J. Kuppers, *Surf. Sci.*, 1978, **76**, 323–342.
42 T. Gießel, O. Schaff, C. J. Hirschmugl, V. Fernandez, K. M. Schindler, A. Theobald, S. Bao, R. Lindsay, W. Berndt,

A. M. Bradshaw, C. Baddeley, A. F. Lee, R. M. Lambert and D. P. Woodruff, *Surf. Sci.*, 1998, **406**, 90–102.
43 M. K. Rose, T. Mitsui, J. Dunphy, A. Borg, D. F. Ogletree, M. Salmeron and P. Sautet, *Surf. Sci.*, 2002, **512**, 48–60.
44 P. Sautet, M. K. Rose, J. C. Dunphy, S. Behler and M. Salmeron, *Surf.Sci.*, 2000, **453**, 25–31.
45 F. M. Hoffmann, *Surf. Sci. Rep.*, 1983, **3**, 107–192.
46 M. Morkel, H. Unterhalt, M. Salmeron, G. Rupprechter and H.-J. Freund, *Surf. Sci.*, 2003, **532–535**, 103–107.
47 G. Rupprechter, H. Unterhalt, M. Morkel, P. Galletto, T. Dellwig and H.-J. Freund, *Vacuum*, 2003, **71**, 83–87.
48 K. Honkala, P. Pirila and K. Laasonen, *Phys. Rev. Lett.*, 2001, **86**, 5942–5945.
49 K. Honkala, P. Pirila and K. Laasonen, *Surf. Sci.*, 2001, **489**, 72–82.
50 H. Conrad, G. Ertl, J. Koch and E. E. Latta, *Surf. Sci.*, 1974, **43**, 462–480.
51 M. Tushaus, W. Berndt, H. Conrad, A. M. Bradshaw and B. Persson, *Appl. Phys. A: Solids Surf.*, 1990, **51**, 91–98.
52 V. V. Kaichev, M. Morkel, H. Unterhalt, I. P. Prosvirin, V. I. Bukhtiyarov, G. Rupprechter and H.-J. Freund, *Surf. Sci.*, 2004, **566–568**, 1024–1029.
53 E. Ozensoy, D. C. Meier and D. W. Goodman, *J. Phys. Chem. B*, 2002, **106**, 9367–9371.
54 H. Unterhalt, G. Rupprechter and H.-J. Freund, *J. Phys. Chem. B*, 2002, **106**, 356–367.
55 P. J. Feibelman, B. Hammer, J. K. Norskov, F. Wagner, M. Scheffler, R. Stumpf, R. Watwe and J. Dumesic, *J. Phys. Chem. B*, 2001, **105**, 4018–4025.
56 P. Lazic, M. Alaei, N. Atodiresei, V. Caciuc, R. Brako and S. Blugel, *Phys. Rev. B: Condens. Matter Mater. Phys.*, 2010, **81**, 045401.
57 A. W. K. Liu and M. B. Santos, *Thin Films: Heteroepitaxial Systems*, World Scientific, Singapore, 1999.
58 L. Brewer, *Report LBL-3720*, 1977.
59 S. J. Guo, S. J. Dong and E. K. Wang, *ACS Nano*, 2010, **4**, 547–555.
60 B. Lim, M. J. Jiang, P. H. C. Camargo, E. C. Cho, J. Tao, X. M. Lu, Y. M. Zhu and Y. N. Xia, *Science*, 2009, **324**, 1302–1305.
61 Z. M. Peng and H. Yang, *J. Am. Chem. Soc.*, 2009, **131**, 7542–7543.